

Nematic Superfluidity and Wigner Crystallization of Bosons in Frustrated Kagome Lattices

Guanyu Zhu,¹ Jens Koch,¹ and Ivar Martin²

¹*Departments of Physics and Astronomy, Northwestern University, Evanston, Illinois 60208, USA*

²*Materials Science Division, Argonne National Laboratory, Argonne, Illinois 60439, USA*

(Dated: December 7, 2024)

We consider a family of tight-binding models based on kagome lattice with local fluxes, which have a lowest flat band in the single particle spectrum. The flat band is spanned by eigenstates forming localized loops on the lattice, with the maximally compact loop states typically breaking the discrete rotational symmetry of the lattice. When populated by locally-interacting particles, the close packing of such maximally compact loop states leads to a nematic Wigner crystal ground state. If particles are bosons, increasing filling beyond the close packing filling fraction, at the mean field level, leads to formation of nematic supersolid and a nematic superfluid phases with broken lattice rotation and $U(1)$ symmetry.

PACS numbers: 67.85.-d, 03.75.Ss.

Introduction.— The problem of interacting bosons in frustrated lattices with a flat band has been a subject of significant theoretical interest [1–7]. Due to the exact degeneracy in the single particle spectrum, there is no preferred momentum state for the Bose condensation to occur and hence novel phases are expected to emerge. With the single-particle kinetic energy quenched, interaction determines how the massive band degeneracy is resolved. This is reminiscent of the physics of the fractional quantum Hall effect, where Coulomb interaction lifts the degeneracy of a partially filled Landau level. Depending on the specific model and parameter regime, bosonic ground states in such frustrated lattices can belong to topological phases and include composite-fermion states of hard-core bosons [7–9], fractional Chern insulators [4, 6], and other exotic broken symmetry states [1–3, 5, 10, 11].

With the rapid advance of artificial condensed matter systems such as cold atoms in optical lattices and interacting photons in circuit-QED lattices, it has become possible not only to realize geometrically frustrated lattices but also lattices subject to synthetic gauge fields [12–23]. Thus, a variety of flat-band interacting boson models can already be engineered with current experimental techniques.

In this letter, we focus on one of the paradigmatic examples of a frustrated lattice – the kagome lattice [1, 5, 8–10, 24–26]. In the context of the Bose-Hubbard model, previous studies have considered this lattice with positive hopping, $|t|$, which produces a flat lowest band. This situation is, however, gapless since the flat band is touched by another band at the Γ point [1, 3, 5]. That makes analysis of interacting problem quite subtle due to the ability of particles to leak easily into the higher band. We show here that the flat band can be gapped off by inserting an additional gauge flux into each hexagon of the kagome lattice. The single-particle eigenstates composing the flat band can be chosen as localized *loop states*, which typically break the rotational C_6 symmetry.

The introduced gap enables a well-controlled projection onto the flat band subspace [1, 27, 28] in the weak-interaction regime, $U \ll |t|$, and yields an effective low-energy Hamiltonian. This is analogous to the lowest-Landau level projection employed in the fractional quantum Hall effect. Depending on

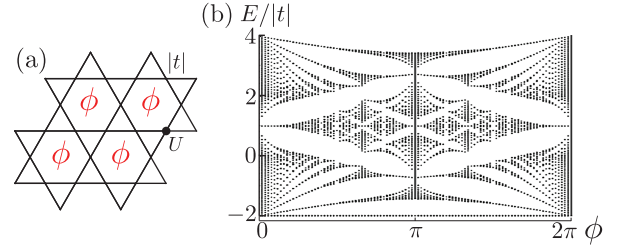


FIG. 1: (color online). (a) Kagome lattice with positive hopping and flux ϕ penetrating each hexagon. (b) Tight-binding energies as a function of ϕ (Hofstadter butterfly). The lowest flat band is gapped for non-integer $\phi/2\pi$ and reaches its maximum gap size at π flux.

the filling fraction of the lattice, we find three types of exotic nematic phases. At close packing of maximally compact loop states, a nematic Wigner crystal forms the exact ground state of the system. In the specific case of π -flux and higher filling fraction, our mean-field treatment predicts transitions to a nematic supersolid followed by a nematic superfluid phase. The possibility of microscopic liquid crystalline phases has been pointed out previously in the context of strongly correlated electronic materials [29, 30]. In this letter, we focus on translationally invariant/periodic states. Additional rich physics is associated with topological defects [31] and warrants future study.

Model.—The Bose-Hubbard model on the kagome lattice subject to gauge flux [Fig. 1] is described by the Hamiltonian

$$H = \sum_{\langle r, r' \rangle} \left(|t| e^{i A_{rr'}} b_{r'}^\dagger b_r + \text{h.c.} \right) + U \sum_r b_r^\dagger b_r^\dagger b_r b_r, \quad (1)$$

where b_r^\dagger creates a single boson on the site labeled r . The first term is the tight-binding Hamiltonian H_{tb} determining the band structure of the non-interacting bosons. We denote the hopping amplitude by $|t|$ to stress that it is positive (frustrated) [36]. The gauge potential $A_{rr'}$ is defined on each nearest-neighbor bond $\langle r, r' \rangle$ and determines the flux $\phi = \sum_{\langle r, r' \rangle} A_{rr'}$ threading each plaquette in the lattice. The second term in H captures the repulsive Hubbard interaction on each site with strength $U > 0$.

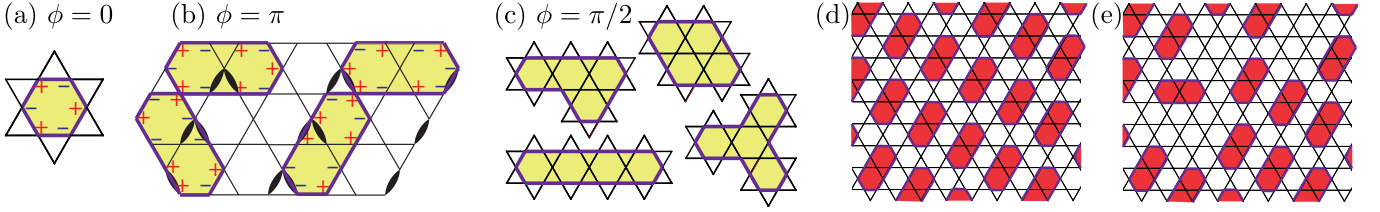


FIG. 2: (color online). (a-c) Maximally compact loop eigenstates for $\phi = 0, \pi$ and $\pi/2$. Thick bonds in (b) mark links with negative hopping $-|t|$. “ \pm ” denotes the sign of the wavefunction amplitude on the corresponding sites. (d) and (e) illustrate the nematic Wigner crystal and hard-core loop gas for $\phi = \pi$.

Gapped flat band in the presence of flux.—We first discuss the tight-binding band structure for $U = 0$. Once flux ϕ is inserted into each hexagon of the kagome lattice, the single-particle spectrum $E(\phi)$ takes the typical Hofstadter butterfly form [Fig. 1]. For non-integer $\phi/2\pi$, the lowest band [37] remains flat but acquires a gap that reaches its maximum size of $\Delta \approx 0.55|t|$ at π flux. At this point, time-reversal (TR) symmetry is intact and the model can be realized with real-valued hopping of positive and negative sign. Energy and degeneracy of the flat band are independent of flux. The latter is given by number of hexagons in the lattice, $N_{\text{site}}/3$ (N_{site} denoting the number of sites).

Localized loop eigenstates.—The presence of the flat band is directly linked to the existence of degenerate eigenstates that form localized loops. The localization mechanism, called caging [32, 33], is due to destructive interference of the wavefunction amplitude anywhere outside the loop [3]. In the kagome lattice with positive hopping, the flat band and localization persist as long as there is no flux through triangles (see S.I for proof).

Previous studies [1, 3, 27, 28] have focused on the zero-flux case and identified the state with amplitudes of equal magnitude but alternating signs on the hexagon loop as the maximally compact eigenstate [see Fig. 2(a)]. While the existence of flat band and localized eigenstates remains unharmed by the flux through hexagons, we find that the shapes of loop states must change. Specifically, in the spirit of a flux-quantization condition, every loop must enclose an integer number of flux quanta, $\phi_L = \sum_{\text{loop}} A_{rr'} = \sum_{\text{loop}} \phi \in 2\pi\mathbb{N}$ (see S.I for proof). For $\phi = \pi$ and $\frac{\pi}{2}$, we show maximally compact loop eigenstates encircling two and four hexagons in Fig. 2(b) and (c), respectively. Note that orientation and shape of maximally compact loop states are not generally unique for $\phi \neq 0$.

The main focus of this letter is the case of flux $\phi = \pi$ where TR symmetry is intact and maximally compact loop states are dimers encircling two hexagons. By a convenient gauge choice $A_{rr'} = \pi$ on decorated bonds [Fig. 2(b)], all hopping elements are real and given by $|t|$ on regular and $-|t|$ on decorated bonds [38]. In this gauge, amplitudes of loop eigenstates simply alternate in sign across positive-hopping bonds and are identical across decorated negative-hopping bonds. In the following, we consider occupation of these states by multiple bosons and refer to the maximally compact loop states as Loop Orbitals (LOs).

Exact nematic Wigner crystal ground state.—We next turn to the interacting case, accounting for on-site boson repulsion due to the Hubbard term $U \sum_r b_r^\dagger b_r^\dagger b_r b_r$. Since the interaction is local, we note that *any* many-body state of the form $\prod_{m \in \mathcal{A}} L_m^\dagger |0\rangle$ with single-particle occupation of a set \mathcal{A} of *non-overlapping* LOs is an exact ground state of the interacting system for filling $\nu = |\mathcal{A}|/N_{\text{site}}$ [39]. Here, the operator L_m^\dagger creates a single particle occupying the LO labeled by m . Indeed, the above product state is an eigenstate with eigenenergy $-2|t|$ per particle and interaction does not contribute since double occupancy of sites is avoided.

Once the filling reaches close packing, the ground state becomes an incompressible Wigner crystal [2]. No additional particle can be placed on the lattice without incurring an interaction-induced energy increase due to unavoidable overlap. At the critical filling ν_c of close packing, bosons occupy maximally compact LOs while avoiding double occupation. As discussed above, maximally compact LOs may break the lattice point group symmetry (here, D_6), which directly leads to ground states with spontaneously broken lattice symmetry.

In general, the filling fraction ν_c for close packing depends on flux. In the π -flux case, maximally compact LOs are dimers and close packing occurs at $\nu_c = 1/15$. Due to the three possible orientations of a dimer [Fig. 2(b)] and the freedom to use one Wigner crystal representative [Fig. 2(d)] and produce four other inequivalent ones by translations to four neighboring hexagons, we predict that the ground state is overall 15-fold degenerate. These ground states are nematic Wigner crystals. Here, nematicity refers to the emergence of dimers that break the lattice rotation symmetry. In this aspect, the π -flux case is dramatically different from the 0-flux case studied before in the context of both the boson model and the antiferromagnetic Heisenberg spin model [40], where the $\nu = 1/9$ Wigner crystal ground state [1, 27, 28] does not exhibit any nematicity. We note that the nematic Wigner crystal state can also be found in the magnetization plateau of the corresponding Heisenberg model in the presence of both positive and negative XY interaction.

We note that for $\phi = \pi$ and filling below ν_c , bosons form an infinitely compressible hard-core loop gas with macroscopic degeneracy determined by all possible configurations of non-overlapping loops [27, 28]. One such configuration is depicted in Fig. 2(e).

Flat-band projection and construction of Wannier or-

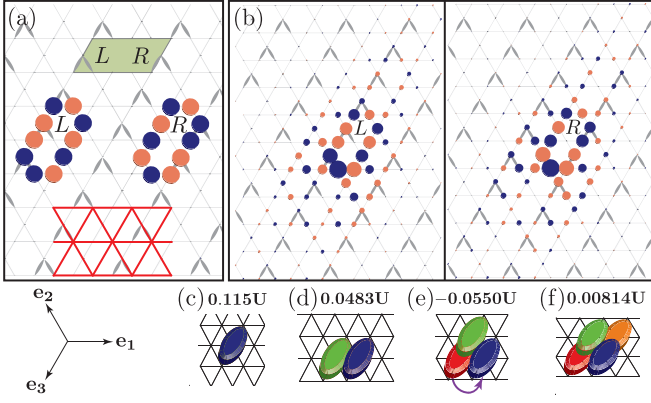


FIG. 3: (color online). (a) The two types of dimer LOs used to construct the Wannier basis. Disks in orange/blue (light/dark gray) represent positive/negative amplitudes of the LO. The shaded area on top shows a single unit cell, containing two hexagons, L and R . The centers of LOs form a triangular lattice (bottom). (b) Two neighboring orthogonal Wannier orbitals. The area of each disk is proportional to the amplitude of the wavefunction on that site. Bottom panels show four types of effective interactions: (c) on-site repulsion, (d) density-density repulsion, (e) assisted-hopping, and (f) ring-exchange.

bitals.—In the following, we exclusively focus on the π -flux case. To treat filling above close packing, we derive a low-energy effective Hamiltonian by adapting the approach by Huber and Altman [1], consisting of a projection onto the subspace spanned by flat-band eigenstates. In our case of nonzero flux, however, we forego the more subtle situation of an ungapped band encountered in [1]. In the presence of a gap and in the weak-interaction limit, boson occupation is to a good approximation limited to the flat band and the projection is appropriate unless the filling fraction becomes too large (details depend on the ratio $U/|t|$).

To facilitate the projection, we construct an orthonormal basis of the flat band. For π flux, the unit cell is doubled and contains a left and right hexagon, L and R , which differ by the relative positions of negative-hopping bonds [Fig. 3(a)]. Due to the unit-cell doubling there are, strictly speaking, two degenerate flat bands. Accordingly, we choose two sets of maximally compact dimer LOs aligned in the \mathbf{e}_3 direction [Fig. 3(a)] as our basis for the two degenerate flat bands. We distinguish left-dimer states only containing L hexagons from right-dimer states only containing R hexagons. Although these sets of LOs together form a basis of the two degenerate flat bands, not all basis states are mutually orthogonal. We thus need to determine appropriate superpositions of the dimer LOs to form a set of mutually-orthogonal Wannier orbitals (WOs). As usual, there is not a unique set of WOs and different choices can vary significantly in their real-space localization. Since we will ultimately employ local-decoupling mean-field theory, it is particularly important to obtain well-localized WOs [41].

Our construction scheme for suitable WOs involves an important step of orthogonalizing the sets of left and right LOs

by means of a symmetrized version of the Gram-Schmidt procedure (see S.III for details). The results for two adjacent WOs are depicted in Fig. 3(b). The major part of the real-valued WO amplitude is essentially concentrated on each original dimer [Fig. 3(a)]. From there, the amplitudes decrease rapidly (asymptotically in an exponential fashion). This is in contrast to the slower power-law decay of WO amplitudes in the 0-flux case which is caused by the touching of bands [1]. The WOs we obtain respect translational symmetry (in terms of probability), TR symmetry, and preserve the mirror symmetry along their major axes, just as the original dimer LOs. They weakly break mirror symmetry along their minor axes.

We define the creation operator for occupation of these Wannier orbitals by $w_j^\dagger \equiv \sum_r w_j(r) b_r^\dagger$, where the Wannier function $w_j(r)$ gives the amplitudes of the dimer-type WO centered at position j of the effective triangular lattice [Fig. 3(a)] on each site r of the underlying kagome lattice. Upon projection and switching to the grand-canonical ensemble, the effective Hamiltonian takes the form

$$H_{\text{eff}} = \sum_j (-2|t| - \mu) w_j^\dagger w_j + \sum_{ijkl} I_{ijkl} w_i^\dagger w_j^\dagger w_k w_l, \quad (2)$$

where μ is the chemical potential. For convenience, we may define the shifted chemical potential $\mu' = \mu + 2|t|$ which absorbs the energy constant of the flat band. The coefficients $I_{ijkl} \equiv U \sum_r w_i^*(r) w_j^*(r) w_k(r) w_l(r)$ determine the strength of the effective interaction terms and involve overlaps of four Wannier functions centered on specific sites i, j, k , and l of the triangular lattice. Due to the localization of WOs, the interaction is short range and falls off rapidly with growing spatial distance between the four sites. We note that I_{ijkl} is translationally invariant and real-valued (since the constructed Wannier functions are real-valued themselves).

The distinct spatial configurations of the four dimer WOs labeled i through l give rise to different types of interaction terms. Whenever all four indices coincide, the contribution corresponds to an effective onsite repulsion $\sum_j U' w_j^\dagger w_j^\dagger w_j w_j$ with strength $U' = I_{jjjj} = 0.11U$. Among the set of all effective interaction terms, this on-site repulsion term has the largest strength. The next sub-leading terms come from two other types of effective interaction, namely density-density repulsion $V_{\text{DD}} = \sum_{i,j} I_{ijij}^\text{d} n_i n_j$ [Fig. 3(d)], and assisted hopping $V_{\text{AH}} = \sum_{i,j} \sum_k I_{ijk}^\text{ah} w_i^\dagger w_j^\dagger w_k$ [Fig. 3(e)]. Here, $n_j \equiv w_j^\dagger w_j$ denotes the Wannier number operator, and the primes on sums signal that those terms with coinciding summation indices are to be omitted. The strengths of density-density interaction and assisted hopping depend on the specific arrangement of the involved WO dimers. The largest contributing terms are $I_{0,\mathbf{e}_1}^\text{d} = 0.0483U$ and $I_{0,\mathbf{e}_1,-\mathbf{e}_3}^\text{ah} = -0.055U$, and thus significantly smaller than the on-site repulsion strength U' .

Within the low-density regime $\nu < 1/3$ (i.e., $\nu_{\text{eff}} < 1$ in the effective triangular lattice), we therefore employ a hard-core approximation which forbids double occupation of WOs [1]. Within this approximation, interaction terms with repeated Wannier operators on the same site, $w_j^\dagger w_j^\dagger$ or $w_j w_j$, drop out.

This includes effective onsite interaction as well as pair hopping $\sum_{i,j} I_{ij} w_i^\dagger w_j^\dagger w_j w_i$. Besides density-density repulsion and assisted hopping, the only remaining interaction type is ring-exchange [Fig. 3(f)], in which the Wannier functions are centered on four different sites on the triangular lattice. We find that the maximum strength of ring exchange is $0.00814U$ which is significantly weaker than both density-density repulsion and assisted hopping.

Mean-field theory.—While density-density repulsion favors density-wave order and formation of a Wigner crystal, assisted hopping may lead to melting and formation of a superfluid. In addition, this competition also allows for an intermediate supersolid phase in which both types of order are present. Here, we study competition between different types of orders within mean-field theory (MFT). We adopt the Gutzwiller approach [34] and employ a product ansatz consistent with the hard-core constraint

$$|\psi_{\text{MF}}\rangle = \prod_j (f_{j,0} + f_{j,1} w_j^\dagger) |0\rangle, \quad (3)$$

which decouples sites on the effective triangular lattice of WOs. The mean-field ansatz naturally captures the nematic Wigner crystal phase since it is a product of single-particle states with occupation of non-overlapping LOs (in this case approximated by WOs). Above close packing, mean-field solutions continue to break the C_6 symmetry due to the anisotropic nature of the Wannier orbitals.

To describe states with density-wave order such as the nematic Wigner crystal, we must allow for the dependence of the mean-field amplitudes $f_{j,n}$ on the spatial index j . To obtain mean-field solutions, we decouple the effective Hamiltonian, replacing density-density interaction and assisted-hopping terms by $V_{\text{DD}} \rightarrow \sum_{i,j} 2I_{ij}^{\text{d}} n_i \langle n_j \rangle$ and $V_{\text{AH}} \rightarrow \sum_{i,j} \sum_k I_{ijk}^{\text{ah}} \langle w_i^\dagger \rangle \langle w_j \rangle n_k + \sum_{i,j} \sum_k I_{ijk}^{\text{ah}} (w_i^\dagger \langle w_j \rangle + \text{h.c.}) \langle n_k \rangle$. (We have verified that inclusion of ring-exchange does not lead to significant changes.) With this, we obtain a mean-field Hamiltonian $\sum_i h_i(\{\psi_j\}, \{n_j\})$ where h_i depends on the mean-field order parameters $\psi_j = \langle w_j \rangle$ and $n_j = \langle n_j \rangle$ on each site of the triangular lattice. Starting from a random initial set of order parameters on a lattice of 200 sites with periodic boundary conditions, we repeatedly solve for the eigenstates and re-calculate order parameters until reaching self-consistency (see S.VI for details).

For a range of chemical potentials, we calculate results for the mean filling $\langle \nu \rangle \equiv \sum_i n_i / N_{\text{site}}$, density-wave order parameter $\langle \chi_{\text{dw}} \rangle$ defined as the difference between maximum and average density taking into account the six surrounding sites, and the mean superfluid order parameter $\langle \psi_{\text{sf}} \rangle \equiv \sum_i \psi_i / N_{\text{site}}$. The key results from this calculation are presented in Figure 4. MFT reproduces the exact nematic Wigner crystal [Fig. 4(b)] for $\mu' \simeq 0.05U$ at close packing $\langle \nu \rangle = 1/15$, showing maximum density-wave order $\langle \chi_{\text{dw}} \rangle = 1$ and vanishing superfluidity $\langle \psi_{\text{sf}} \rangle = 0$. Below close packing, MFT produces a gradual change of average filling and superfluid order, which differs from the known exact solution based on LOs. The exact solution exhibits a density plateau at ν_c containing the entire nematic Wigner crystal phase, and a vertical

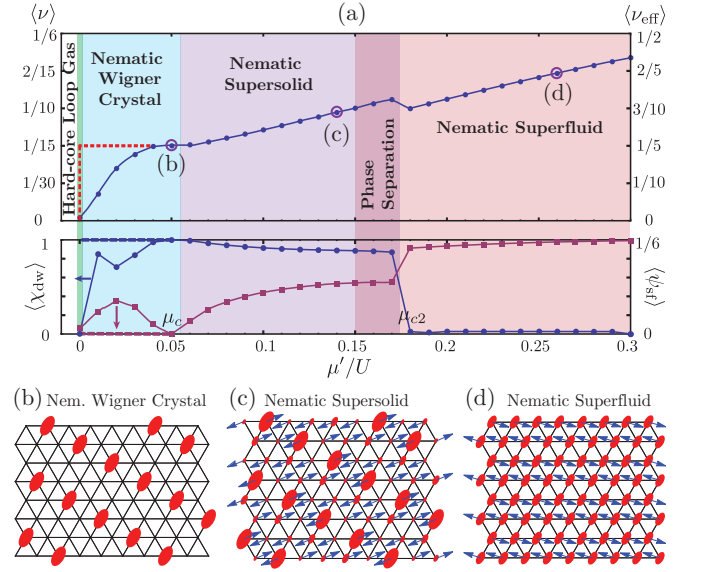


FIG. 4: (color online). (a) Mean-field phase diagram and plot of average density $\langle \nu \rangle$, $\langle \nu_{\text{eff}} \rangle$ on the effective triangular lattice, average density-wave order $\langle \chi_{\text{dw}} \rangle$ (blue dots) and average superfluid order $\langle \psi_{\text{sf}} \rangle$ (red squares) versus chemical potential. Dashed lines show the exact solution with LOs. (b-d) Results from MFT for ground states in the three phases. The area of depicted dimers is proportional to the local occupation number n_i , arrows show the phase angle θ_i . Results are obtained for a lattice of 200 sites using a self-consistency calculation.

jump corresponding to the hard-core loop gas phase which is more appropriately represented in the canonical ensemble.

Above μ_c , superfluid order sets in and $\langle \psi_{\text{sf}} \rangle$ grows gradually while, at the same time, the density-wave order parameter $\langle \chi_{\text{dw}} \rangle$ remains nonzero and decays slowly, overall suggesting a second-order transition to a nematic supersolid [Fig. 4(c)] in which a fraction of the bosons condense on interstitial sites between the Wigner-crystal structure. Further on at $\mu_{c2} \simeq 0.18U$, the density-wave order $\langle \chi_{\text{dw}} \rangle$ abruptly drops to zero, accompanied by a sudden increase in the superfluid order $\langle \psi_{\text{sf}} \rangle$. This indicates a sudden melting of the Wigner-crystal structure and a first-order transition into a superfluid phase [Fig. 4(d)].

Based on our MFT, we predict that the superfluid phase is nematic since condensation of bosons is based on hopping among anisotropic dimer WOs. Within the superfluid phase, phase angles $\theta_i = \text{Arg}[\psi_i]$ form stripes in which neighboring stripes differ by a π -phase difference. The nematicity is not only encoded in the microscopic wavefunction, but can also be identified through a macroscopic quantity, the superfluid stiffness tensor: $\rho_{IJ} = \frac{\partial^2 E}{\partial \Delta \theta_I \partial \Delta \theta_J} |_{\Delta \theta_{I,J}=0}$. Here, $\Delta \theta_I$ and $\Delta \theta_J$ represent the phase difference applied to the sample boundary along directions I and J (e.g. \mathbf{e}_1 and \mathbf{e}_3 directions). In this case, ρ_{II} differs from ρ_{JJ} (see S.VII for details), which implies anisotropic superflow and hence breaking of discrete rotational symmetry. The nematic supersolid has similar phase stripes, the only difference being that sites with maximum density have an additional π -phase flip. Fi-

nally, we find a narrow region in which non-monotonic dependence of the density on chemical potential suggests phase coexistence between the superfluid and supersolid.

Summary and outlook— We have studied the emergence of nematic phases in a kagome lattice with a gapped flat band, obtained when a flux π is threaded through each hexagon of the lattice. Single-particle localized loop states can be combined to construct many-body eigenstates below a critical filling. This critical filling corresponds to close packing of non-overlapping loop states and marks the formation of a nematic Wigner crystal ground state. For larger filling, the effective Hamiltonian based on flat-band projection using dimer-shaped Wannier orbitals and subsequent mean-field theory predict nematic supersolid and superfluid phases. Interesting future directions include the study of phases at higher density, especially the possibility of a featureless Mott insulator [35] at $1/3$ filling, resonating valence bond states and fermionized ground states in the strong-interaction regime.

We are indebted to Steven Girvin, Ashvin Vishwanath, Tigran Sedrakyan, Eliot Kapit, Hakan Tureci, Anupam Garg, James Sauls and C. Y. Li for insightful discussions. Work performed at Northwestern University (G.Z. and J.K.) is supported by the NSF under Grant PHY-1055993. Work performed at Argonne National Laboratory (I.M.) is supported by the U. S. Department of Energy, Office of Science, Office of Basic Energy Sciences, under Contract No. DE-AC02-06CH11357.

-
- [1] S. D. Huber and E. Altman, Phys. Rev. B **82**, 184502 (2006).
 - [2] C. Wu, D. Bergman, L. Balents, and S. Das Sarma, Physical review letters **99**, 070401 (2007).
 - [3] D. Bergman, C. Wu, and L. Balents, Phys. Rev. B **78**, 125104 (2008).
 - [4] Y.-F. Wang, Z.-C. Gu, C.-D. Gong, and D. N. Sheng, Physical review letters **107**, 146803 (2011).
 - [5] Y.-Z. You, Z. Chen, X.-Q. Sun, and H. Zhai, Physical review letters **109**, 265302 (2012).
 - [6] Y.-F. Wang, H. Yao, C.-D. Gong, and D. N. Sheng, Phys. Rev. B **86**, 201101 (2012).
 - [7] T. A. Sedrakyan, L. I. Glazman, and A. Kamenev, Phys. Rev. B **89**, 201112 (2014).
 - [8] K. Yang, L. Warman, and S. Girvin, Phys. Rev. Lett. **70**, 2641 (1993).
 - [9] K. Kumar, K. Sun, and E. Fradkin, arXiv:1409.2171 (2014).
 - [10] D. A. Huse and A. D. Rutenberg, Physical Review B **45**, 7536 (1992).
 - [11] G. Möller and N. R. Cooper, Physical Review A **82**, 063625 (2010).
 - [12] D. Jaksch and P. Zoller, New J. Phys. **5**, 56 (2003).
 - [13] J. Dalibard, F. Gerbier, G. Juzeliūnas, and P. Öhberg, Rev. Mod. Phys. **83**, 1523 (2011).
 - [14] N. Goldman, G. Juzeliūnas, P. Öhberg, and I. B. Spielman, arXiv:1308.6533 (2013).
 - [15] F. Gerbier and J. Dalibard, New Journal of Physics **12**, 033007 (2010).
 - [16] Y. J. Lin, K. Jimenez-Garcia, and I. B. Spielman, Nature **470**, 83 (2012).
 - [17] M. Aidelsburger, M. Atala, M. Lohse, J. T. Barreiro, B. Paredes, and I. Bloch, Physical review letters **111**, 185301 (2013).
 - [18] S.-C. Ji, J.-Y. Zhang, L. Zhang, Z.-D. Du, W. Zheng, Y.-J. Deng, H. Zhai, S. Chen, and J.-W. Pan, Nature Physics **10**, 314 (2014).
 - [19] G. Jotzu, M. Messer, R. Desbuquois, M. Lebrat, T. Uehlinger, D. Greif, and T. Esslinger, arXiv:1406.7874 (2014).
 - [20] J. Koch, A. A. Houck, K. Le Hur, and S. M. Girvin, Physical Review A **82**, 043811 (2010).
 - [21] A. Nunnenkamp, J. Koch, and S. M. Girvin, New Journal of Physics **13**, 095008 (2011).
 - [22] M. Hafezi, S. Mittal, J. Fan, A. Migdall, and J. M. Taylor, Nature Photonics (2013).
 - [23] M. Hafezi and P. Rabl, Optics express **20**, 7672 (2012).
 - [24] S. Sachdev, Phys. Rev. B **45**, 12377 (1992).
 - [25] L. Balents, M. P. A. Fisher, and S. M. Girvin, Phys. Rev. B **65**, 224412 (2002).
 - [26] M. Punk, D. Chowdhury, and S. Sachdev, Nature Physics **10**, 289 (2014).
 - [27] M. Zhitomirsky and H. Tsunetsugu, Phys. Rev. B **70**, 100403 (2004).
 - [28] M. E. Zhitomirsky and H. Tsunetsugu, Prog. Theor. Phys. Suppl. **160**, 361. 22 p (2005).
 - [29] S. A. Kivelson, E. Fradkin, and V. J. Emery, Nature **393**, 550 (1998).
 - [30] R. M. Fernandes, A. V. Chubukov, and J. Schmalian, Nat Phys **10**, 97 (2014).
 - [31] P. G. de Gennes and J. Prost, *The Physics of Liquid Crystals* (Oxford University Press; 2nd edition, August 10, 1995).
 - [32] J. Vidal, R. Mosseri, and B. Douçot, Physical review letters **81**, 5888 (1998).
 - [33] W. Häusler, arXiv:1407.6286 (2014).
 - [34] D. S. Rokhsar and B. G. Kotliar, Physical Review B **44**, 10328 (1991).
 - [35] S. A. Parameswaran, I. Kimchi, A. M. Turner, D. M. Stamper-Kurn, and A. Vishwanath, Physical review letters **110**, 125301 (2013).
 - [36] In ultracold-atom experiments, the natural negative hopping can be turned positive by threading triangles of the kagome lattice with a π flux.
 - [37] The term “band” is applied loosely here. For rational flux, the unit cell is enlarged and the flat band decomposes into multiple ones. No such simple picture applies to irrational flux.
 - [38] Circuit QED lattices including both positive and negative hopping can be realized by a clever choice of resonator modes (see S.II).
 - [39] Note: for filling below close packing, there will generally be a large number of degenerate ground states.
 - [40] Note: the Wigner crystal state, termed as valence-bond crystal in the spin context, is also the exact ground state corresponding to the $7/9$ magnetization plateau of the antiferromagnetic kagome Heisenberg model in an external magnetic field. This model is equivalent to a hard-core boson model with additional nearest-neighbor density-density repulsion. For the non-overlapping loop configuration, both the onsite and nearest-neighbor repulsion is avoided, which leads to zero interaction energy cost.
 - [41] Note: it is possible to construct C_6 symmetric but less compact localized orbitals as our flat-band basis. However, the mean-field ansatz with such orbitals has much larger interaction energy cost due to larger overlap and hence is not energetically favorable (see S.IV for details).

Supplemental Material

S.I LOOP EIGENSTATES AND “FLUX QUANTIZATION”

We list three important properties for the single particle eigenstates in the flat band of the tight-binding kagome Hamiltonian:

1. The energy of the single particle eigenstate is exactly $-2|t|$ [can be directly observed from the butterfly spectrum Fig.1(b)]
2. The elementary flat-band eigenstates are single-particle “loop” states which have equal probability on each involved site. The amplitudes on the adjacent sites outside the loop (on the outward and inward triangles) cancel due to destructive interference (“caging”). Any other flat band state can be composed as a linear superposition of loop states.
3. “Flux quantization”: a loop eigenstate encloses integer number of flux quanta (2π).

Properties 2 and 3 can be derived from property 1 as follows. The positive-hopping tight-binding lattice Hamiltonian in the presence of gauge field A has the form:

$$H_{tb} = \sum_{\langle j,j' \rangle} |t| e^{iA_{jj'}} b_{j'}^\dagger b_j + \text{H.c.} \equiv \sum_{\langle j,j' \rangle} T_{jj'}, \quad (\text{S1})$$

where $T_{jj'}$ is the hopping operator on the nearest-neighbor bond $\langle j, j' \rangle$. Assuming that there exists single-particle wavefunction of the loop eigenstate, it can be expressed as

$$|\psi_L\rangle = \sum_{j \in L} \psi_j b_j^\dagger |0\rangle, \quad (\text{S2})$$

where the summation index j runs over all sites on the loop L . When acting with the Hamiltonian H_{tb} on the loop eigenstates, we can split the expressions into two parts, namely

$$H_{tb}|\psi_L\rangle = \sum_{\langle j,j' \rangle \in L} T_{jj'}|\psi_L\rangle + \sum_{\langle j,j' \rangle \in L, k \notin L} [T_{jk} + T_{j'k}]|\psi_L\rangle. \quad (\text{S3})$$

The first sum includes hopping along the bonds $\langle j, j' \rangle$ on the loop L , while the second sum corresponds to hopping from the bonds $\langle j, j' \rangle$ on the loop to the adjacent sites k on the outward/inward triangles, as illustrated in Fig.S1. The cancellation of the probability amplitude outside the loop (caging, rule 2) requires the second sum to be zero, while the requirement of eigenenergy being $-2|t|$ (rule 1) implies that:

$$\sum_{\langle j,j' \rangle \in L} T_{jj'}|\psi_L\rangle \equiv \sum_{\langle j,j' \rangle \in L} |t| [e^{iA_{jj'}} \psi_j b_{j'}^\dagger + e^{-iA_{jj'}} \psi_{j'} b_j^\dagger] |0\rangle = -2|t| |\psi_L\rangle \equiv \sum_{\langle j,j' \rangle \in L} -|t| [\psi_{j'} b_j^\dagger + \psi_j b_{j'}^\dagger] |0\rangle. \quad (\text{S4})$$

This equation can be satisfied by imposing equality of the left and right hand sides on every bond. This leads to a “chain rule” of the single particle wavefunction,

$$\psi_{j'} = -\psi_j e^{iA_{jj'}}. \quad (\text{S5})$$

That is, the wavefunction has equal probability on every site along the loop, and the adjacent sites differ by a minus sign and an additional phase shift due to the gauge potential $A_{jj'}$ living on the bond $\langle j, j' \rangle$. When applying the “chain rule” [Eq. (S5)] around the loop and requiring the probability amplitude ψ_j to be single-valued, we derive the “flux quantization” condition of a loop eigenstate (property 3), namely

$$\phi_L = \sum_{\langle j,j' \rangle} A_{jj'} = 2\pi n, \quad n \in \mathbb{N}. \quad (\text{S6})$$

Here, the direction of the gauge potentials $A_{jj'}$ is chosen to be counterclockwise (\odot) around the loop L . Now we consider the cancellation of the second sum in Eq. (S3) which leads to “caging”, and get

$$[T_{jk} + T_{j'k}]|\psi_L\rangle = |t| [e^{iA_{jk}} \psi_j b_k^\dagger + e^{-iA_{j'k}} \psi_{j'} b_k^\dagger + \text{H.c.}] |0\rangle = 0, \quad (\text{S7})$$

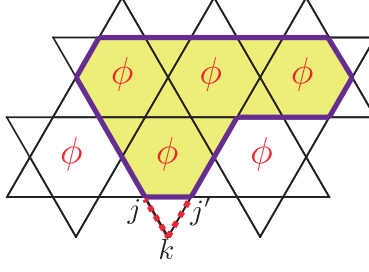


FIG. S1: (color online). Illustration of a general single-particle loop eigenstate, where j and j' label the sites on the loop, and k labels the site outside the loop where destructive interference occurs.

which leads to $\psi_{j'} = -\psi_j e^{i(A_{jk} + A_{kj'})}$. Combined with Eq. (S5), we get

$$\phi_\Delta = A_{jk} + A_{kj'} + A_{j'j} = 0. \quad (\text{S8})$$

Thus, we have just proved the prerequisite of the existence of lowest flat band with energy $-2|t|$, which is our starting argument that the flux threading all the outward/inward triangles must be zero (gauge-equivalent to π -flux in the negative hopping model).

Up to now, we have derived property 3, and part of property 2 (namely the existence and properties of the flat-band loop eigenstates). The completeness of the loop states, which means the loop states form a basis for the flat band, is to be discussed in S.III.

One can see from the above derivation that the existence of flat band and localized loop states is not limited to “uniform” flux into each hexagon. In general, loop eigenstates with eigenenergy $-2|t|$ exist and can compose an entire flat band as long as the “flux quantization” condition is satisfied.

Now we consider the gauge-invariant current operator on the bond $\langle j, j' \rangle$ (from site j to site j'), namely,

$$J_{jj'} = 2|t|i[b_{j'}^\dagger b_j e^{iA_{jj'}} - \text{H.c.}]. \quad (\text{S9})$$

Its expectation value is given by,

$$\langle \psi_L | J_{jj'} | \psi_L \rangle = 2|t|i[\psi_{j'}^* \psi_j e^{iA_{jj'}} - \text{H.c.}], \quad (\text{S10})$$

which equals to zero after applying the “chain rule” [Eq. (S5)]. Therefore, for any flux value ϕ , the loop states in the flat band carries no current, and thus breaks no time-reversal (TR) symmetry, even though the Hamiltonian itself breaks TR except at $\phi = 0, \pi$. From the butterfly spectrum, we observe that the lowest flat band does not change as a function of ϕ , which leads to zero current due to the linear response formula of the current $J = \frac{\partial E}{\partial \phi} = 0$. The fact that there is no current can also be understood in another way, i.e. the Chern number for the lowest flat band is always zero. This is in contrast to the higher bands near $\phi = 0$ [Fig.2(b)], which are essentially Landau levels with nonzero Chern numbers $C = 1, 2, 3$, etc..

S.II REALIZATION OF THE π -FLUX MODEL WITH PHOTON LATTICE BASED ON CIRCUIT-QED ARCHITECTURE

Although in principle one can introduce synthetic gauge flux to realize any gapped flat-band model discussed in the main text, it is worthwhile to point that one can realize the π -flux model simply with both positive and negative hopping bonds, and without the requirement of an actual gauge field. For photon lattice, engineering different hopping signs can be easily achieved by cleverly choosing proper resonator modes.

Specifically, photon lattices based on circuit-QED (cQED) elements have been realized in recent experiments and are under rapid development [S1–S4, S21]. The photon lattices are formed by two-end superconducting resonators (labeled by j) with frequency ω , coupled capacitively to each other in the form of $(\pm)_{jj'} C_c V_j V_{j'}$. Here, $C_c > 0$ is the coupling capacitance and V_j and $V_{j'}$ denote the voltages of the two adjacent resonators on the ends where they contact each other. The sign $(\pm)_{jj'}$ is equal to the product of the signs of the mode functions on each end, i.e. $(\pm)_{jj'} = \text{sgn}[\phi_j(x)\phi_{j'}(x')|_{\text{ends}}]$ [21]. The possible gauge-equivalent configurations depend on the mode choice of the resonators. As an example, for the λ -mode which has the same signs on the two ends, one can easily choose positive signs for both ends, and make all hopping signs positive $(\pm)_{jj'} \rightarrow +$. Canonical quantization of the Voltage leads to the definition of photon operator b_j for a chosen mode of the resonator at site j through $V_j = V_0(b_j + b_j^\dagger)$, where V_0 has the dimension of Voltage and is determined by the capacitance and mode structure of

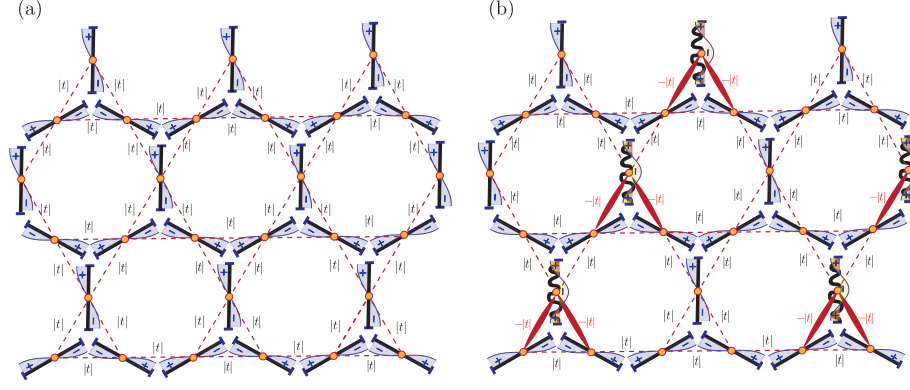


FIG. S2: (color online). Circuit-QED realization of the frustrated kagome lattices. (a) Realization of positive-hopping model with 0-flux. The two-ended resonators (black lines) form a honeycomb array, of which the dual lattice is the actual kagome photon lattice. The kagome lattice sites are represented by yellow circles and the bonds by red dashed lines. The mode functions are illustrated with blue shades, where the signs on the ends are shown. The photon hopping amplitudes are shown on the bonds and being all positive in the $\lambda/2$ -mode case, since the signs of the mode functions can be chosen the same at each three-way junction. (b) Realization of the π -flux model. Certain resonators are replaced by wiggling resonators with twice of the original length and hence correspond to the λ mode. For a particular gauge choice, all the signs on the ends of the mode functions are shown. All the bonds represented by the dashed lines still have positive hopping ($|t|$), while decorated bonds (ellipses) have negative hopping ($-|t|$).

the resonators. A superconducting qubit with frequency ϵ is placed in each resonator and interact with the resonator through Jaynes-Cummings interaction $g(a_j^\dagger \sigma_j^- + a_j \sigma_j^+)$ [S3, S4]. In the dispersive regime ($g \ll \epsilon - \omega$), the qubit can be integrated out via the Schrieffer-Wolff transformation [S5, S6] which yields an effective Hubbard interaction $U b_j^\dagger b_j^\dagger b_j b_j$. This effective interaction has been experimentally observed and termed as dispersive photon blockade [S7]. One can also think of qubits as nonlinear medium which effectively introduces Kerr nonlinearity to the resonators. Hence, the entire Hamiltonian which describes the photon lattice is as follows:

$$H = \omega \sum_j b_j^\dagger b_j + |t| \sum_{j,j'} (\pm)_{jj'} [b_j^\dagger b_{j'} + \text{H.c.}] + \sum_j U b_j^\dagger b_j^\dagger b_j b_j, \quad (\text{S11})$$

which is nothing but the Bose-Hubbard Hamiltonian. The first frequency term is just a constant shift of energy and can be absorbed into the definition of chemical potential. The hopping strength $|t|$ is proportional to the coupling capacitance C_c . The possible gauge-equivalent sign configurations $(\pm)_{jj'}$ are determined by the choice of modes. The many-body physics of interacting photons can be studied in the context of either quasi-equilibrium with engineered chemical potential for photons [S8, S9], or dissipative phase transitions of the non-equilibrium steady-states [S10, S11].

As shown in Fig. S2, the two-end resonators (black lines) are coupled equally to their neighboring two by the three-way capacitors and form a Honeycomb array. The actual photon lattice is its graphic dual: the kagome lattice (shown by red dashed lines), where the lattice sites (yellow dots) reside effectively in the center of the two-end resonators. The qubits are put in these lattice sites in order to introduce nonlinearity to the resonators and create effective Hubbard interaction.

We first consider $\lambda/2$ mode for each resonator, which has the lowest frequency and hence is relevant for the ground/low-lying states. As shown in Fig. S2(a), one can choose a particular gauge configuration, in which all the mode functions have the same signs (either positive or negative) on the ends as the other two that coupled at the three-way junction. Thus, the photon hoppings across the bonds (represent by dashed lines) in this gauge are made all positive throughout the whole lattice, which means there is a lowest flat-band for the photon tight-binding model. However, in this case, the flat band has band touching with the higher dispersive band at Γ point as discussed in Ref. [1].

To open a gap above the flat band, we need to introduce gauge flux into the hexagons as discussed in the main text. The π -flux model can be simply realized by making a lattice with both $\lambda/2$ - and λ -mode resonators as shown in Fig. S2(b), where the wiggling lines represent resonators with twice the length of the straight resonators in the manner of actual experimental implementation [S3]. The ground/low-lying states will only involve $\lambda/2$ mode in the straight resonators and λ mode in the wiggling resonators. A particular gauge configuration for the mode function is shown in Fig. S2(b). This leads to the hopping configurations that all the bonds (red dashed lines) correspond to positive hopping ($|t|$), and all the decorated bonds (red ellipses) have an additional π -gauge potential and hence are equivalent to negative hopping ($-|t|$). This achieves exactly the same gauge for π -flux model as we mentioned in the main text.

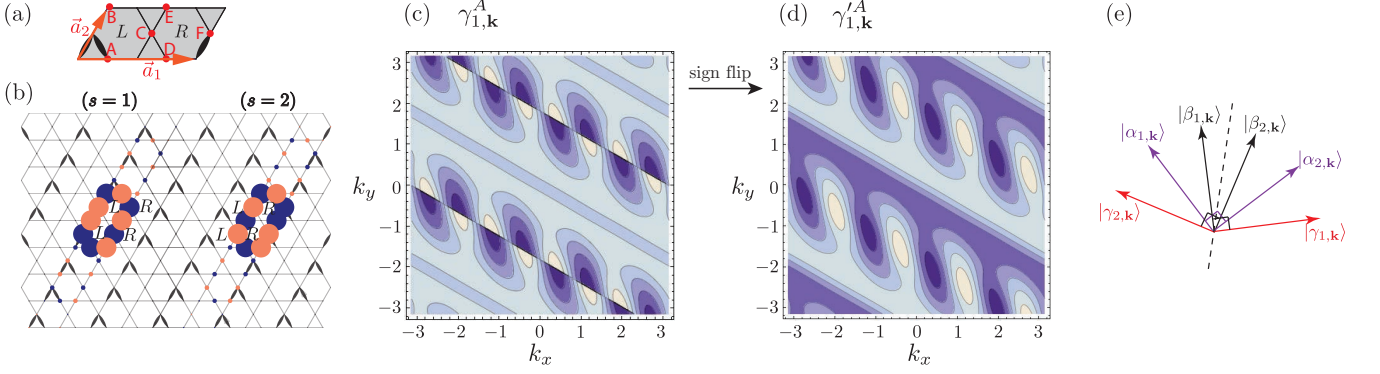


FIG. S3: (color online). (a) The unit cell of the π -flux kagome lattice, which contains two hexagons and six sites. (b) Illustration of two Wannier functions transformed from the two Bloch vectors $\vec{\beta}_{1,\mathbf{k}}$ and $\vec{\beta}_{2,\mathbf{k}}$ via Eq. (S16). (c) The contour plot which shows the distribution of the A-component of the Bloch vector $\gamma_{1,\mathbf{k}}$ in \mathbf{k} -space. There are diagonal discontinuity cuts in the \mathbf{k} -space. (d) The improved distribution in panel (c) after a sign flip in every other strip. Now the discontinuities are removed. (e) Illustration of the symmetrized Gram-Schmidt process.

S.III CONSTRUCTION OF ORTHOGONAL WANNIER ORBITALS

For the π -flux case, the unit cell is doubled with respect to the 0-flux case and hence includes 6 sites (labeled as A, B, C, D, E, and F), as shown in Fig. S3(a). Hence, the lowest flat bands are doubly degenerate, which means that there is an arbitrary choice to decompose the two flat bands, since for each \mathbf{k} one can arbitrarily choose two orthogonal Bloch vectors in the 2-dimensional degenerate subspace. Sensible choice of basis has to be physically motivated and has to respect certain symmetries.

For the sake of convenience, we choose loops along the \mathbf{e}_3 -direction as our preferred flat band basis (total number $N_{\text{site}}/3$ equals the number of flat-band degeneracy). The operators $L_{s,\mathbf{R}}^\dagger$ which create the two types of loops within each unit cell can be represented by the original lattice boson operators as:

$$\begin{aligned} L_{1,\mathbf{R}}^\dagger &= b_{\mathbf{R}}^{A\dagger} - b_{\mathbf{R}}^{B\dagger} + b_{\mathbf{R}}^{C\dagger} - b_{\mathbf{R}}^{E\dagger} - b_{\mathbf{R}-\mathbf{a}_2}^{E\dagger} - b_{\mathbf{R}-\mathbf{a}_1+\mathbf{a}_2}^{F\dagger} + b_{\mathbf{R}+\mathbf{a}_2}^{B\dagger} - b_{\mathbf{R}+2\mathbf{a}_2}^{A\dagger} + b_{\mathbf{R}+\mathbf{a}_2}^{C\dagger}, \\ L_{2,\mathbf{R}}^\dagger &= b_{\mathbf{R}+\mathbf{a}_1}^{B\dagger} - b_{\mathbf{R}+\mathbf{a}_1-\mathbf{a}_2}^{B\dagger} - b_{\mathbf{R}}^{C\dagger} - b_{\mathbf{R}+\mathbf{a}_2}^{C\dagger} + b_{\mathbf{R}}^{D\dagger} - b_{\mathbf{R}+2\mathbf{a}_2}^{D\dagger} + b_{\mathbf{R}}^{E\dagger} + b_{\mathbf{R}+\mathbf{a}_2}^{E\dagger} - b_{\mathbf{R}}^{F\dagger} + b_{\mathbf{R}+\mathbf{a}_2}^{F\dagger}. \end{aligned} \quad (\text{S12})$$

Here, the index $s = 1, 2$ labels the loops encircling left/right hexagons. The wavefunctions of the two types of loops are already shown in Fig. 3(a). Here, the lattice vectors $\mathbf{R} \equiv (m, n)$ labels the enlarged 6-site unit cell and the lattice vectors $\mathbf{a}_1 \equiv (1, 0)$ and $\mathbf{a}_2 \equiv (0, 1)$ translate the cells in the two oblique directions [shown in Fig. S3(a)].

One can construct two classes of Bloch states by translationally-invariant superposition (with a particular wavevector \mathbf{k}) of the two types of loop states respectively, i.e.

$$L_{s,\mathbf{k}}^\dagger = \sum_{\mathbf{R}} e^{-i\mathbf{k}\cdot\mathbf{R}} L_{s,\mathbf{R}}^\dagger. \quad (\text{S13})$$

Here, left/right label $s=1, 2$ can also be thought as the band index and in this particular case labels the two degenerate flat bands. The generated state $L_{s,\mathbf{k}}^\dagger |0\rangle = \sum_l u_{s,\mathbf{k}}^l b_{\mathbf{k}}^{l\dagger} |0\rangle$ can be represented by a 6-component Bloch vector $\vec{u}_{s,\mathbf{k}}$, where we have $l=A, B, \dots, F$ and $b_{\mathbf{k}}^{l\dagger} = \sum_{\mathbf{R}} e^{-i\mathbf{k}\cdot\mathbf{R}} b_{\mathbf{R}}^{l\dagger}$. The two Bloch vectors got from the two chosen loop states are represented as

$$\begin{aligned} \vec{u}_{1,\mathbf{k}} &= (1 - e^{-i2\mathbf{k}\cdot\mathbf{R}_2}, -1 + e^{-i\mathbf{k}\cdot\mathbf{R}_2}, 1 + e^{-i\mathbf{k}\cdot\mathbf{R}_2}, 0, -1 - e^{-i\mathbf{k}\cdot\mathbf{R}_2}, e^{i\mathbf{k}\cdot\mathbf{R}_1} - e^{i\mathbf{k}\cdot(\mathbf{R}_1-\mathbf{R}_2)})^T, \\ \vec{u}_{2,\mathbf{k}} &= (0, e^{-i\mathbf{k}\cdot\mathbf{R}_1} - e^{-i\mathbf{k}\cdot(\mathbf{R}_1-\mathbf{R}_2)}, -1 - e^{-i\mathbf{k}\cdot\mathbf{R}_2}, 1 - e^{-i2\mathbf{k}\cdot\mathbf{R}_2}, 1 + e^{-i\mathbf{k}\cdot\mathbf{R}_2}, -1 - e^{-i\mathbf{k}\cdot\mathbf{R}_2})^T. \end{aligned} \quad (\text{S14})$$

However, the Bloch vector $\vec{u}_{s,\mathbf{k}}$ is not yet normalized. We call the normalized Bloch vectors $\vec{\beta}_{s,\mathbf{k}}$, and define the normalized Bloch state as $|\beta_{s,\mathbf{k}}\rangle = \tilde{L}_{s,\mathbf{k}}^\dagger |0\rangle = \sum_l \beta_{s,\mathbf{k}}^l b_{\mathbf{k}}^{l\dagger} |0\rangle$, where the redefined operator $\tilde{L}_{s,\mathbf{k}}^\dagger$ now becomes canonical Bosonic operators satisfying the commutation relation $[\tilde{L}_{s,\mathbf{k}}, \tilde{L}_{s,\mathbf{k}'}^\dagger] = \delta_{\mathbf{k},\mathbf{k}'}$. Thus, we get a set of orthonormal Bloch states for each of the two flat bands, and can be transformed into two sets of Wannier states as:

$$\mathbf{w}_{s,\mathbf{R}}^\dagger = \frac{1}{\sqrt{N_{\text{site}}}} \sum_{\mathbf{k}} e^{i\mathbf{k}\cdot\mathbf{R}} \tilde{L}_{s,\mathbf{k}}^\dagger \equiv \sum_{\mathbf{R}', l} w_{s,\mathbf{R}}^l(\mathbf{R}') b_{\mathbf{R}'}^{l\dagger}, \quad (\text{S15})$$

where the Wannier wavefunction is given by

$$w_{s,\mathbf{R}}^l(\mathbf{R}') = \frac{1}{\sqrt{N_{\text{site}}}} \sum_{\mathbf{k}} e^{i\mathbf{k}\cdot\mathbf{R}} \beta_{s,\mathbf{k}}^l e^{-i\mathbf{k}\cdot\mathbf{R}'} . \quad (\text{S16})$$

Here, the Wannier wavefunction sits on the coordinate (\mathbf{R}', l) . The coordinate (\mathbf{R}, s) labels where the center of the wavefunction locates. We note that the more detailed notations, $w_{s,\mathbf{R}}^\dagger$ and $w_{s,\mathbf{R}}^l(\mathbf{R}')$, which we use here, are equivalent to the more compact notations we have used in the main text, namely w_j^\dagger and $w_j(r)$. The direct correspondence is $r \equiv (\mathbf{R}', l)$ and $j \equiv (\mathbf{R}, s)$. The two sets of wavefunctions are illustrated in Fig. S3(b), where the $s=1$ one encircles only the left hexagons in every unit cell and the $s=2$ one encircles only the right hexagons. The major part of the real-valued Wannier functions are essentially the two dimer loop states which we start with. The amplitude tail spreads out and decays exponentially along the major axis of the loop which ensures orthogonalization. However, the two sets of Wannier functions are not mutually orthogonal to each other (for example, those neighboring ones will still have finite overlap) since the two sets of Bloch vectors are not mutually orthogonalized yet.

For each \mathbf{k} , one can orthogonalize the two Bloch vectors through the Gram-Schmidt process, i.e.

$$|\gamma_{1,\mathbf{k}}\rangle = \frac{|\beta_{2,\mathbf{k}}\rangle - |\beta_{1,\mathbf{k}}\rangle\langle\beta_{1,\mathbf{k}}|\beta_{2,\mathbf{k}}\rangle}{\| |\beta_{2,\mathbf{k}}\rangle - |\beta_{1,\mathbf{k}}\rangle\langle\beta_{1,\mathbf{k}}|\beta_{2,\mathbf{k}}\rangle \|}, \quad (\text{S17})$$

which generates a normalized $|\gamma_{1,\mathbf{k}}\rangle$ orthogonal to $|\beta_{1,\mathbf{k}}\rangle$. Similarly, one can get a normalized $|\gamma_{2,\mathbf{k}}\rangle$ which is orthogonal to $|\beta_{2,\mathbf{k}}\rangle$. Therefore, one can choose either orthogonal pair as the flat-band basis. However, from either choice, the acquired Wannier wavefunctions belonging to the two bands have completely different shapes and hence lose translational symmetry. To preserve translational symmetry and being closer to a dimer shape, we can make a symmetric superposition as:

$$|\alpha_{1,\mathbf{k}}\rangle = \frac{1}{\sqrt{2}} [|\beta_{1,\mathbf{k}}\rangle + e^{i\theta_{\mathbf{k}}}|\gamma_{2,\mathbf{k}}\rangle], \quad |\alpha_{2,\mathbf{k}}\rangle = \frac{1}{\sqrt{2}} [|\beta_{2,\mathbf{k}}\rangle + e^{i\theta_{\mathbf{k}}}|\gamma_{1,\mathbf{k}}\rangle], \quad (\text{S18})$$

where $|\alpha_{1,\mathbf{k}}\rangle$ and $|\alpha_{2,\mathbf{k}}\rangle$ are the mutually-orthogonal sets of Bloch states we choose. The additional free choice of phase factor $e^{i\theta_{\mathbf{k}}}$ will give rise to different Wannier states. The sensible choice of the phase factor makes sure that the Bloch vectors are analytically continuous in \mathbf{k} -space, which ensures that the generated Wannier function is exponentially localized [S12] and hence is more compact.

The Bloch states generated from the Gram-Schmidt process, $|\gamma_{s,\mathbf{k}}\rangle$, are unfortunately not analytically continuous. For example, as shown in Fig. S3(c), the A -component of one of the Bloch vectors, $\gamma_{1,\mathbf{k}}^A$, has a diagonal discontinuity cut in its real part. Same cut happens for its imaginary part and most of the other components of $|\gamma_{1,\mathbf{k}}\rangle$, and $|\gamma_{2,\mathbf{k}}\rangle$.

Thus, one has to take advantage of the additional phase factor $e^{i\theta_{\mathbf{k}}}$ to remove the discontinuity. In this particular case, a simple sign flip of every other strip in the k -space, which can be expressed as a square-wave function: $\text{sgn}[\sin[(k_x, k_y) \cdot (1, \sqrt{3})]]$, is able to remove the discontinuity [see Fig. S3(d)]. In addition, we employ an extra phase factor $e^{i\mathbf{k}\cdot\mathbf{a}_2}$ to ensure no breaking of TR symmetry and closeness in shape to the dimer loop state. Thus, our choice of phase factor $e^{i\theta_{\mathbf{k}}}$ for Eq. (S18) is $e^{i\mathbf{k}\cdot\mathbf{a}_2} \text{sgn}[\sin[(k_x, k_y) \cdot (1, \sqrt{3})]]$ (a \mathbf{k} -independent relative sign or phase factor does not affect the probability distribution of the Wannier functions). This particular choice yields the complete Wannier basis illustrated in Fig. 3(b).

Our Wannier Orbitals (WOs) preserve the mirror symmetry (in terms of probability) with respect to its major axis, similar to the original Loop Orbitals (LOs) which they are based on. However, due to the additional phase factor we choose to keep the analytical continuity, the mirror symmetry along the minor axis is slightly broken. We can see that the lower part of the WO has slightly larger probability than the upper part. If we replace part of the phase factor $e^{i\mathbf{k}\cdot\mathbf{a}_2}$ with $e^{-i\mathbf{k}\cdot\mathbf{a}_2}$, the shape of the WO will be flipped with respect to the minor axis, namely the higher part will have larger probability. We also note that we do not claim that we have found the maximally compact WOs, even though the construction is based on the maximally compact LOs. In general, it should be possible to numerically/analytically determine such maximally compact WO which also preserve both types of mirror symmetries. Thus, our current approach is just a simple mathematical construction which aims to approximate the maximally compact WOs, since the shape we have acquired is not too far from the original LOs which they are based on.

Finally we note that, since we have successfully found a complete orthogonal Bloch or Wannier basis from superposition of the dimer loop states, we have proved the completeness of the loop states which is mentioned in property 2 of section S.I.

S.IV LOCALIZED ORBITALS PRESERVING C_6 SYMMETRY

We show that it is possible to construct a localized orbital which preserve the C_6 rotational symmetry of probability. The most compact C_6 -symmetric orbital can be constructed by the superposition of six dimer loop orbitals as shown in Fig. S4. In panel (a), we have six dimer loop orbitals (with the amplitude labeled for each site) sharing the same left hexagon. The superposition

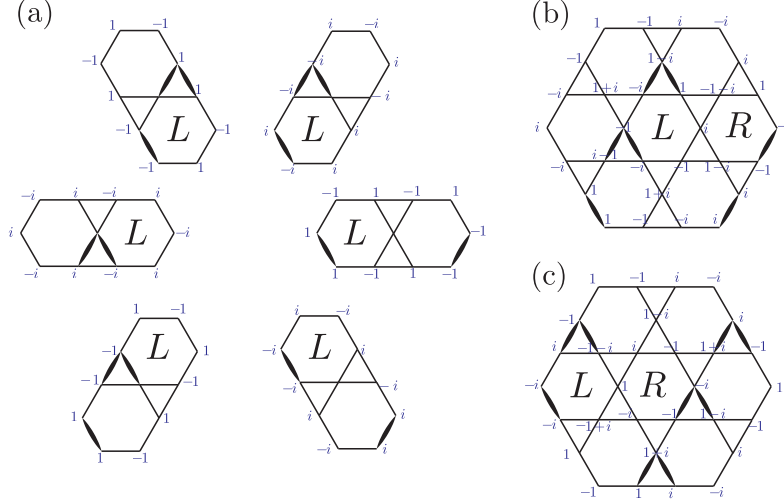


FIG. S4: (color online). (a) Six dimer loop orbitals (with amplitudes labeled for each site) sharing the same left hexagon. (b) A C_6 -symmetric localized orbital centered on the left hexagon. The orbital is superimposed by the six dimer loop orbitals in panel (a). (c) A C_6 symmetric localized orbital centered on the right hexagon. The orbital has the same probability distribution as the one in panel (b).

of the six orbitals generate a C_6 -symmetric orbital in panel (b), centered on the left hexagon. We note that in order to preserve the C_6 -symmetry of probability, one has to introduce relative phase between the orbitals, and in this example a $\pi/2$ phase. This leads to the imaginary number i in certain amplitudes and breaking of TR symmetry. In this case, another possible choice is obtained by turning i into $-i$. This orbital also preserves the C_6 -symmetry and has the opposite current. The reason of this is that the C_6 -symmetric orbital includes seven (odd number) π -fluxes, which gives rise to the doubly degenerate eigenstates with opposite chirality. A similar construction can generate a C_6 -symmetric orbital centered on the right hexagon, by the superposition of the six surrounding dimer loops. Thus, for each hexagon, one can generate a C_6 -symmetric orbital centered on right hexagons with the same probability distribution. These orbitals form a complete and spatially uniform basis of the gapped flat band and can also be orthogonalized to form Wannier orbitals.

The reason that we do not choose these C_6 -symmetric orbitals as our basis for flat-band projection and mean-field theory is that they have much larger overlaps compared to the dimer loop orbitals. Therefore, at low density ($\nu < 1/3, \nu_{\text{eff}} < 1$) when the hard-core approximation holds, a mean-field product state of particles occupying such orbitals, in the form of $|\psi_{\text{MF}}\rangle = \prod_j (f_{j,0} + f_{j,1} w_j^\dagger) |0\rangle$, will cause much more interaction energy than using more compact and anisotropic orbitals, and hence is not energetically favorable. However, when going up to high density ($\nu \gg 1/3, \nu_{\text{eff}} \gg 1$), namely on average more than 1 particle per orbital, the hard-core approximation breaks down and there will be large interaction energy cost for particles in the same orbital. Hence there is no obvious advantage for particles to occupy more compact orbitals. Thus, one may expect a phase transition from nematic phase to isotropic (also chiral) phase at high filling, which will be studied more systematically in future works.

S.V SUMMARY OF TERMS IN THE EFFECTIVE HAMILTONIAN

Here we classify all types of effective interaction $\sum_{ijkl} I_{ijkl} w_i^\dagger w_j^\dagger w_k w_l$, not limited by the hard-core constraint. The types of terms are listed below:

(1) On-site repulsion:

$$V_{\text{on-site}} = \sum_j U' w_j^\dagger w_j^\dagger w_j w_j, \quad (\text{S19})$$

where $U' = I_{jjjj} \approx 0.11U$ is the largest energy scale in the effective Hamiltonian.

(2) Density-density repulsion:

$$V_{\text{DD}} = \sum_{(i,j)} 2I_{ij}^d w_i^\dagger w_i w_j^\dagger w_j = \sum_{i,j}' I_{ij}^d w_i^\dagger w_i w_j^\dagger w_j, \quad (\text{S20})$$

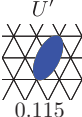
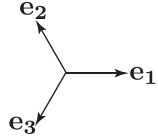
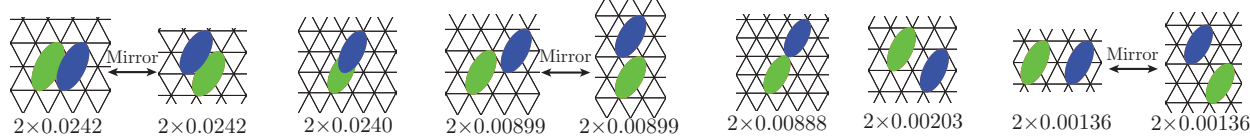
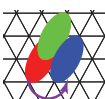
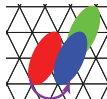
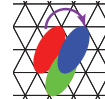
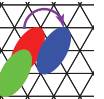
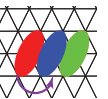
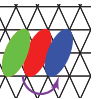
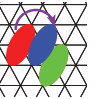
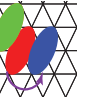
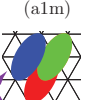
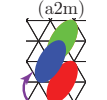
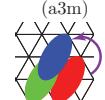
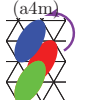
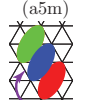
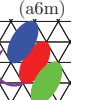
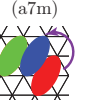
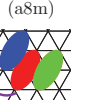
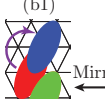
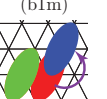
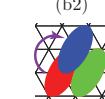
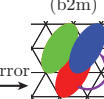
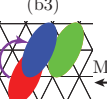
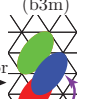
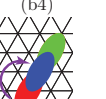
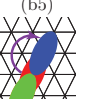

<div>I. Onsite Repulsion: $\sum_j U' w_j^\dagger w_j^\dagger w_j w_j$</div> <div><p>0.115</p></div>	
<div>II. Density-Density Repulsion: $\sum_{i,j} I_{ij}^d w_i^\dagger w_i^\dagger w_j^\dagger w_j$</div> <div></div>	
<div>III. Assisted hopping terms: $\sum_{i,j,k} I_{ijk}^{ah} w_i^\dagger w_j^\dagger w_k^\dagger w_k$</div> <div>(a). NN Hopping term 1 :</div> <div><div><div><p>-0.0138x4</p></div><div><p>-0.00850x4</p></div><div><p>-0.00250x4</p></div><div><p>0.00177x4</p></div><div><p>0.00139x4</p></div><div><p>0.00365x4</p></div><div><p>0.00330x4</p></div><div><p>0.00179x4</p></div><div><p>0.0138x4</p></div><div><p>0.00850x4</p></div><div><p>0.00250x4</p></div><div><p>-0.00177x4</p></div><div><p>0.00139x4</p></div><div><p>0.00365x4</p></div><div><p>-0.00330x4</p></div><div><p>-0.00179x4</p></div></div><div><div><p>0.00358x4</p></div><div><p>-0.00358x4</p></div><div><p>0.00774x4</p></div><div><p>-0.00774x4</p></div><div><p>0.0101x4</p></div><div><p>-0.0101x4</p></div><div><p>0</p></div><div><p>0</p></div></div></div>	
<div>IV. Ring-exchange interaction: $\sum_{(i,j),(k,l)} I_{ij,kl}^{\text{Ring}} (w_i^\dagger w_j^\dagger w_k^\dagger w_l + \text{H.c.})$</div> <div></div>	

FIG. S5: (color online). Table summarizing the leading terms and their coefficients (in units of Hubbard interaction strength U) of the effective onsite repulsion and the other three types of effective interactions which survive under the hard-core constraint.

where (i, j) means sum over pairs of sites ($i \neq j$). Thus, (i, j) and (j, i) correspond to the same term and should not be double counted. Now we determine the coefficients I_{ij}^d of the effective interaction. Four terms in the effective interaction correspond to the pair (i, j) , namely $I_{ijji} w_i^\dagger w_j^\dagger w_j w_i + I_{ijij} w_i^\dagger w_j^\dagger w_i w_j + I_{jiji} w_j^\dagger w_i^\dagger w_j w_i + I_{jiij} w_j^\dagger w_i^\dagger w_i w_j = 4I_{ijji} w_i^\dagger w_i^\dagger w_j^\dagger w_j$. Thus, we get $I_{ij}^d = 2I_{ijji}$.

(3a) Onsite pair-hopping (involving two different sites):

$$V_{\text{PHa}} = \sum_{(i,j)} I_{ij}^p (\mathbf{w}_i^\dagger \mathbf{w}_i^\dagger \mathbf{w}_j \mathbf{w}_j + \text{H.c.}) = \sum'_{i,j} I_{ij}^p \mathbf{w}_i^\dagger \mathbf{w}_i^\dagger \mathbf{w}_j \mathbf{w}_j, \quad (\text{S21})$$

where $I_{ij}^p = I_{ijjj}$.

(3b) Off-site pair-hopping (involving three different sites):

$$V_{\text{PHb}} = \sum_{(i,j)} \sum_{k \neq i,j} [I_{ijk}^p (\mathbf{w}_i^\dagger \mathbf{w}_j^\dagger + \mathbf{w}_j^\dagger \mathbf{w}_i^\dagger) \mathbf{w}_k \mathbf{w}_k + \text{H.c.}] = \sum'_{i,j,k} I_{ijk}^p [\mathbf{w}_i^\dagger \mathbf{w}_j^\dagger \mathbf{w}_k \mathbf{w}_k + \text{H.c.}], \quad (\text{S22})$$

where $I_{ijk}^p = I_{ijkk}$.

(4a) Assisted-hopping (involving three different sites):

$$V_{\text{AHa}} = \sum_{(i,j)} \sum_{k \neq i,j} I_{ijk}^{\text{ah}} (\mathbf{w}_i^\dagger \mathbf{w}_j \mathbf{w}_k^\dagger \mathbf{w}_k + \text{H.c.}) = \sum'_{i,j,k} I_{ijk}^{\text{ah}} \mathbf{w}_i^\dagger \mathbf{w}_j \mathbf{w}_k^\dagger \mathbf{w}_k. \quad (\text{S23})$$

Four terms (and their H.c.) in the effective interaction correspond to the pair (i, j) , namely $I_{ikjk} \mathbf{w}_i^\dagger \mathbf{w}_k^\dagger \mathbf{w}_j \mathbf{w}_k + I_{ikkj} \mathbf{w}_i^\dagger \mathbf{w}_k^\dagger \mathbf{w}_k \mathbf{w}_j + I_{kijj} \mathbf{w}_k^\dagger \mathbf{w}_i^\dagger \mathbf{w}_j \mathbf{w}_k + I_{kiji} \mathbf{w}_k^\dagger \mathbf{w}_i^\dagger \mathbf{w}_k \mathbf{w}_j = 4I_{ikjk} \mathbf{w}_i^\dagger \mathbf{w}_j \mathbf{w}_k^\dagger \mathbf{w}_k$. Thus, we get $I_{ijk}^{\text{ah}} = 4I_{ikjk}$ ($i \neq j \neq k$).

(4b) Assisted-hopping (involving only two different sites):

$$V_{\text{AHb}} = \sum_{(i,j)} [I_{ijj}^{\text{ah}} (\mathbf{w}_i^\dagger \mathbf{w}_j + \text{H.c.}) \mathbf{w}_j^\dagger \mathbf{w}_j + I_{jii}^{\text{ah}} (\mathbf{w}_i^\dagger \mathbf{w}_j + \text{H.c.}) \mathbf{w}_i^\dagger \mathbf{w}_i] = \sum'_{i,j} I_{ijj}^{\text{ah}} (\mathbf{w}_i^\dagger \mathbf{w}_j + \text{H.c.}) \mathbf{w}_j^\dagger \mathbf{w}_j. \quad (\text{S24})$$

Here, we have $I_{ijj}^{\text{ah}} = 2I_{ijjj}$, due to the presence of two terms of each type, e.g. $I_{ijjj} \mathbf{w}_i^\dagger \mathbf{w}_j \mathbf{w}_j^\dagger \mathbf{w}_j + I_{jjjj} \mathbf{w}_j^\dagger \mathbf{w}_j \mathbf{w}_i^\dagger \mathbf{w}_j = 2I_{ijjj} \mathbf{w}_i^\dagger \mathbf{w}_j \mathbf{w}_j^\dagger \mathbf{w}_j$.

(5) Ring-exchange interaction:

$$V_{\text{Ring}} = \sum_{(i,j),(k,l)} I_{ij,kl}^{\text{Ring}} (\mathbf{w}_i^\dagger \mathbf{w}_j^\dagger \mathbf{w}_k \mathbf{w}_l + \text{H.c.}). \quad (\text{S25})$$

Here, $\sum_{(i,j),(k,l)}$ means each term in the sum selects two pair of sites (none of the four sites coincide), one pair with creation operators and the other pair with annihilation operators. Due to the fact that (i, j) and (j, i) correspond to the same thing, there are $2 \times 2 = 4$ terms from effective interaction correspond to the same type. Thus, we get $I_{ij,kl}^{\text{Ring}} = 4I_{ijkl}$. Note that, for each plaquette (i, j, k, l) , there are $\binom{4}{2} = 4$ different types of terms, due to the different choices of creation and annihilation operators.

After imposing the hard-core approximation, namely replacing the Wannier operators \mathbf{w}_j^\dagger by the Pauli operator σ_j^+ , only the density-density repulsion (2), assisted hopping involving three different sites (4a) and the ring-exchange interaction (5) survive. Other types of term vanish due to the doubling of Pauli operators on the same site, namely $(\sigma_j^+)^2 = 0$. We list the leading terms of these types in Fig. S5.

There are certain pairs of effective terms illustrated in Fig. S5 which are associated with a mirror reflection along the major axis (\mathbf{e}_3). For the density-density repulsion, terms in such pair have exactly the same coefficients. For the assisted hopping, terms in the mirror pair have the same magnitude for coefficients, but may have opposite signs. In particular, for the assisted hopping in row (b) (hopping along the major axis \mathbf{e}_3), terms in all the mirror pairs have opposite signs. One can see that for uniform density case (e.g. nematic superfluid) and within the mean-field approximation, the assistive number operator of the dimer (green) can be replaced by a constant number. Thus, the mirror terms will cancel out exactly and there will be no effective hopping along the major axis (\mathbf{e}_3) of the dimer. The finite effective hopping of the dimers only occur in the other two directions (\mathbf{e}_1 and \mathbf{e}_2). Therefore, in a nematic superfluid, the hopping of the bosons is anisotropic.

S.VI DETAILS OF THE SELF-CONSISTENCY MEAN-FIELD THEORY ON A LARGE LATTICE

With the decoupling of effective interaction mentioned in the main text, we search for the self-consistent solution on a large periodic lattice (torus) with randomized initial distribution of the mean-field order parameters. We use a local update algorithm: (1) randomly pick up a site i in each step and find the local ground state $|g\rangle_i$ of the decoupled Hamiltonian $h_i(\{\psi_j\}, \{n_j\})$; (2) Calculate the expectation values of the corresponding Wannier operator and Wannier number operator and use them as

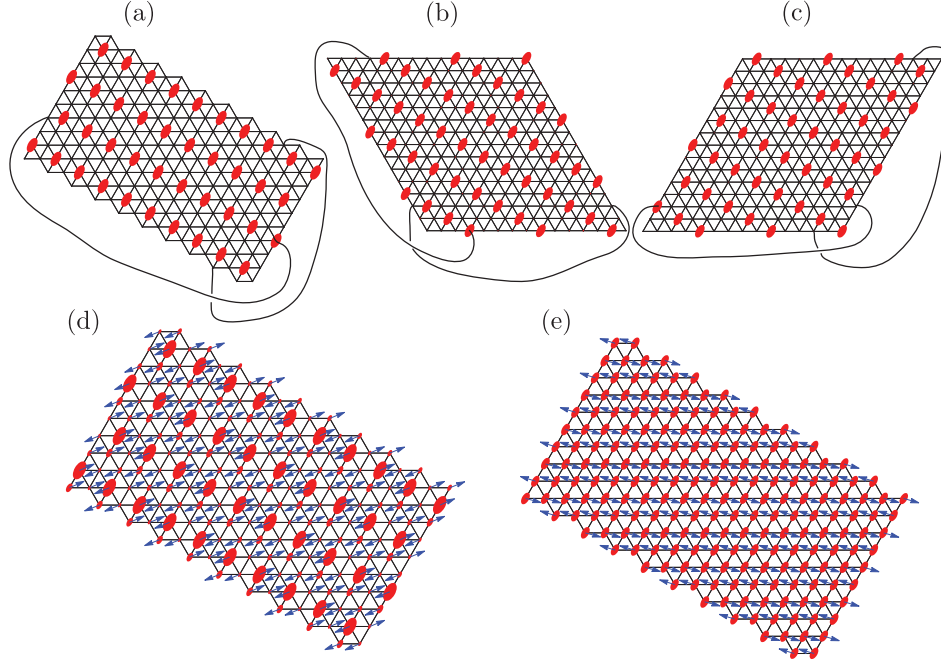


FIG. S6: (color online). (a,b,c) The nematic Wigner crystal ground states from self-consistent mean-field calculations on three different lattices. The periodic boundary condition is illustrated by the wires. The lattices contain 200, 225 and 225 sites respectively. (d,e) The nematic supersolid and nematic superfluid states calculated from the self-consistent mean-field theory on the periodic lattice shown in panel (a).

updated order parameters for site i , i.e. $\psi_i = \langle g | w_i | g \rangle_i$ and $n_i = \langle g | n_i | g \rangle_i$; (3) Repeat the previous two steps until the order parameters on each site have converged and hence reach the self-consistent mean-field solution.

We have done calculations on lattice with different types of geometry, as shown in Fig. S6(a-c) (with the periodic boundary conditions illustrated by the wires). For all the cases, the nematic Wigner crystal states are produced (as shown in the figure), as well as the other two phases. However, the convergence time of the simulation differs from the lattice geometry. We find lattice (a) has the fastest convergence, possibly due to the fact that it respects the mirror symmetry of the dimers along their major axis. Therefore, we use lattice (a) to calculate all the curves shown in Fig. 4(a). For each chemical potential, we do several independent simulations with different randomized initial conditions and pick the one with the lowest energy as our solution. This is due to the fact that sometimes the configuration may be trapped in certain local energy minimum and stop evolving into the true mean-field solution. The complete image of the simulation results (a nematic supersolid state and a nematic superfluid state) from Fig. 4(c,d) is shown in Fig. S6(d,e).

S.VII SUPERFLUID STIFFNESS TENSOR AND NEMATICITY

To better understand the nematicity of the superfluid phase, we consider the superfluid stiffness tensor $\rho_{IJ} = \frac{\partial^2 E}{\partial \Delta \theta_I \partial \Delta \theta_J} |_{\Delta \theta_{I,J}=0}$, where $I, J = 1, 3$ refer to the directions along \mathbf{e}_1 and \mathbf{e}_3 . Note that \mathbf{e}_3 direction is special because it aligns with the major axis of the dimers. To study this quantity, we apply phase differences $\Delta \theta_1$ and $\Delta \theta_3$ across the boundaries of the finite sample (16×16), as shown in Fig. S7(a).

The phase differences across the boundaries induce superflow in the corresponding directions and hence increase the kinetic energy. The contour plot in panel (b) shows the mean-field energy as a function of the phase differences, namely $E(\Delta \theta_1, \Delta \theta_3)$. The superfluid stiffness tensor corresponds to the curvature of the energy profile in the vicinity of the origin. The anisotropy of the energy contours suggests that the superfluid stiffness is also anisotropic. To see this more clearly, we make cuts along the x- and y-axis (blue solid and red dashed line). We then show the energy profile along the two cuts, namely $E(\Delta \theta_1, 0)$ and $E(0, \Delta \theta_3)$, in panel (c). It is obvious that, in the vicinity of the origin, the curvature of the blue solid line is larger than that of the red dashed line, which means that $\rho_{11} \equiv \frac{\partial^2 E}{\partial \Delta \theta_1^2} |_{\Delta \theta_1=0}$ is larger than $\rho_{33} \equiv \frac{\partial^2 E}{\partial \Delta \theta_3^2} |_{\Delta \theta_3=0}$. This suggests that the superfluid stiffness along the two directions is different. Now we consider the first derivative, $j_I \equiv \frac{\partial E}{\partial \Delta \theta_I}$, which is the current generated when applying a phase difference at direction I . We can see that, not far away from the origin, j_1 is always larger than j_3 . This is not surprising since from S.VI we already know that the effective nearest-neighbor hopping along the major axis (\mathbf{e}_3 direction)

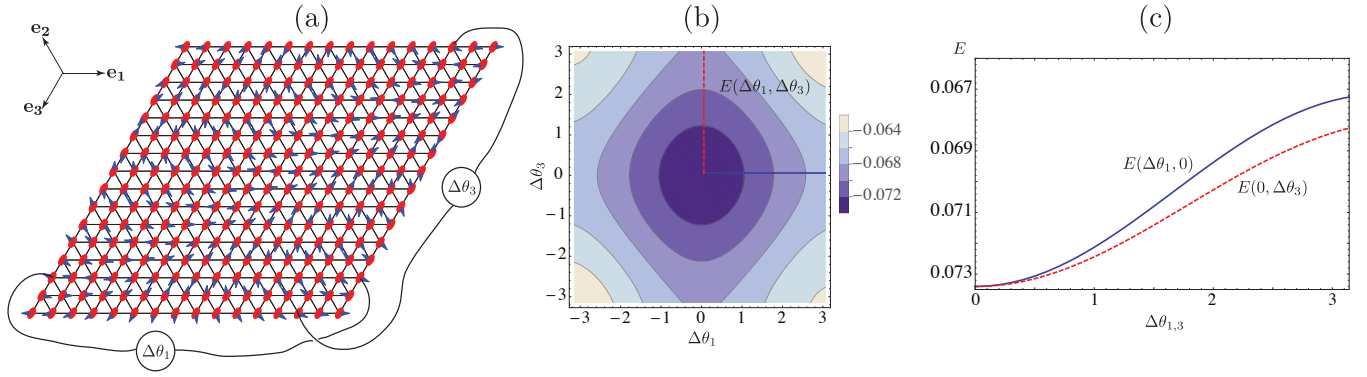


FIG. S7: (color online). (a) Applying phase differences $\Delta\theta_1$ (in the \mathbf{e}_1 direction) and $\Delta\theta_3$ (in the \mathbf{e}_3 direction) across the boundaries of the finite sample (16×16). The configuration of phase angles illustrates the situation of $\Delta\theta_1 = \Delta\theta_3 = \pi$. (b) Contour plot showing the mean-field energy distribution as a function of the phase differences, i.e. $E(\Delta\theta_1, \Delta\theta_3)$. The energy profiles along the two cuts (blue solid and red dashed lines), $E(\Delta\theta_1, 0)$ and $E(0, \Delta\theta_3)$, are shown in panel (c).

is zero in the nematic superfluid phase (within mean-field approximation). Only successive hopping along other directions will contribute to superflow in the \mathbf{e}_3 direction. On the other hand, the large effective nearest-neighbor hopping in the other two directions (\mathbf{e}_1 and \mathbf{e}_2) leads to larger superflow in those directions.

In sum, the anisotropy of the two macroscopic quantities, the superfluid stiffness and superflow, reveals breaking of discrete rotational symmetry and hence microscopic nematicity of the superfluid phase. We note that another kind of probe for nematicity, in the context of ultra-cold atoms, is the time-of-flight experiment, which can reveal the anisotropic property of the correlation function of the ground state. We leave the discussion of this type of experiment to our future work.

-
- [S1] D. L. Underwood, W. E. Shanks, J. Koch, and A. A. Houck, *Physical Review A* **86**, 023837 (2012).
[S2] J. Raftery, D. Sadri, S. Schmidt, H. E. Tureci, and A. A. Houck, *Physical Review X* **4**, 031043 (2014).
[S3] A. A. Houck, H. E. Tureci, and J. Koch, *Nature Physics* **8**, 292 (2012).
[S4] S. Schmidt and J. Koch, *Annalen der Physik* **525**, 395 (2013).
[S5] G. Zhu, S. Schmidt, and J. Koch, *New Journal of Physics* **15**, 115002 (2013).
[S6] G. Zhu, D. G. Ferguson, V. E. Manucharyan, and J. Koch, *Phys. Rev. B* **87**, 024510 (2013).
[S7] A. J. Hoffman, S. J. Srinivasan, S. Schmidt, L. Spietz, J. Aumentado, H. E. Tureci, and A. A. Houck, *Physical review letters* **107**, 053602 (2011).
[S8] M. Hafezi, P. Adhikari, and J. M. Taylor, *arXiv:1405.5821* (2014).
[S9] E. Kapit, M. Hafezi, and S. H. Simon, *Physical Review X* **4**, 031039 (2014).
[S10] A. Tomadin, V. Giovannetti, R. Fazio, D. Gerace, I. Carusotto, H. E. Tureci, and A. Imamoglu, *Physical Review A* **81**, 061801 (2010).
[S11] E. M. Kessler, G. Giedke, A. Imamoglu, S. F. Yelin, M. D. Lukin, and J. I. Cirac, *Physical Review A* **86**, 012116 (2012).
[S12] W. Kohn, *Physical Review B* **7**, 4388 (1973).